TRIM: Triangulating Images for Efficient Registration

Chun Pang Yung, Gary Pui-Tung Choi, Ke Chen, and Lok Ming Lui

arXiv:1605.06215v1 [cs.GR] 20 May 2016

***Abstract*—With the advancement in the digital camera technology, the use of high resolution images and videos has been widespread in the modern society. In particular, image and video frame registration is frequently applied in computer graphics and film production. However, the conventional registration approaches usually require long computational time for high quality images and video frames. This hinders the applications of the registration approaches in the modern industries. In this work, we propose a novel approach called *TRIM* to accelerate the computations of the registration by triangulating the images. More specifically, given a high resolution image or video frame, we compute an optimal coarse triangulation which captures the important features of the image. Then, the computation of the registration can be simplified with the aid of the coarse triangulation. Experimental results suggest that the computational time of the registration is significantly reduced using our triangulation-based approach, meanwhile the accuracy of the registration is well retained when compared with the conventional grid-based approach.**

***Index Terms*—Triangulated Image, image registration, coarse triangulation**

I. Introduction

In recent decades, the rapid development of the digital camera hardware has revolutionized human lives. On one hand, even mid-level mobile devices can easily produce high resolution images and videos. Besides the physical elements, the widespread use of the images and videos also reflects the importance of developing software technology for them. On the other hand, numerous registration techniques for images and video frames have been developed for a long time. The existing registration techniques work well on problems with a moderate size. However, when it comes to the current high quality images and videos, most of the current registration techniques suffer from extremely long computations. This limitation in software seriously impedes fully utilizing the state-of-the-art camera hardware.

One possible way to accelerate the computation of the registration is to introduce a much coarser grid on the images or video frames. Then, the registration can be done on the coarse grid instead of the high resolution images or video frames. Finally, the fine details can be added back to the coarse registration. It is noteworthy that the quality of the coarse grid strongly affects the quality of the final registration result. If the coarse grid cannot capture the important features of the images or video frames, the final registration result is likely to be unsatisfactory. In particular, for the conventional rectangular coarse grids, since the partitions are restricted in the vertical and horizontal directions, important features such as slant edges and irregular shapes cannot be effectively recorded. By contrast, triangulations allow more freedom in the partition directions as well as the partition sizes. Therefore, it is more desirable to make use of triangulations in simplifying the registration problems.

In this work, we propose a novel content-aware algorithm to *TR*iangulate *IM*ages, abbreviated as *TRIM*, that largely simplifies the registration problem for high quality images and video frames. Specifically, given a possibly very high definition image or video frame, we compute a coarse triangulation representation of it. The computation involves a series of steps including subsampling, unsharp masking, segmentation and sparse feature extraction for locating sample points on important features. Then, a high quality triangulation can be created on the set of the sample points using the Delaunay triangulation. With a coarse triangular representation of the images, the registration problem can be significantly accelerated. We apply a landmark-based quasi-conformal registration algorithm [17] for computing the coarse registration. Finally, the fine detail of the image or video frame is computed with the aid of the coarse registration result. Our proposed framework also serves as a highly efficient and accurate initialization for many different registration approaches.

The rest of this paper is organized as follows. In Section II, we review the literature on image and triangular mesh registration. In Section III, we highlight the contribution of our work. Our proposed method is explained in details in Section IV. In Section V, we demonstrate the effectiveness of our approach with numerous real images. The paper is concluded in Section VI.

II. Previous works

In this section, we describe the previous works closely related to our work.

Image registration have been widely studied by different research groups. Surveys on the existing image registration approaches can be found in [34], [5], [16]. In particular, one common approach for guaranteeing the accuracy of the registration is to make use of landmark constraints. Bookstein [1], [2], [3] proposed the unidirectional landmark thin-plate spline (UL-TPS) image registration. In [13], Johnson and Christensen presented a landmark-based consistent thin-plate spline (CL-TPS) image registration algorithm. In [14], Joshi et al. proposed the Large Deformation Diffeomorphic

Department of Mathematics, The Chinese University of Hong Kong. Email:{cpyung,ptchoi,lmlui}@math.cuhk.edu.hk

Department of Mathematical Sciences, The University of Liverpool. Email: k.chen@liverpool.ac.uk

Metric Mapping (LDDMM) for registering images with a large deformation. In [10], [11], Glaunès et al. computed large deformation diffeomorphisms of images with prescribed displacements of landmarks.

A few works on image triangulations have been reported. In [8], Gee et al. introduced a probabilistic approach to the brain image matching problem and described the finite element implementation. In [15], Kaufmann et al. introduced a framework for image warping using the finite element method. The triangulations are created using the Delaunay triangulation method [28] on a point set distributed according to variance in saliency. In [18], [19], Lehner et al. proposed a data-dependent triangulation scheme for image and video compression. Recently, a commercial triangulation image generator called DMesh [6] has been designed.

In our work, we handle image registration problems with the aid of triangulations. Numerous algorithms have been proposed for the registration of triangular meshes. In particular, the landmark-driven approaches use prescribed landmark constraints to ensure the accuracy of mesh registration. In [31], [21], [30], Wang et al. proposed a combined energy for computing a landmark constrained optimized conformal mapping of triangular meshes. In [22], Lui et al. used vector fields to represent surface maps and computed landmark-based close-to-conformal mappings. Shi et al. [29] proposed a hyperbolic harmonic registration algorithm with curvature-based landmark matching on triangular meshes of brains. In recent years, quasi-conformal mappings have been widely used for feature-endowed registration [32], [33], [23], [25]. Choi et al. [4] proposed the FLASH algorithm for landmark aligned harmonic mappings by improving the algorithm in [31], [21] with the aid of quasi-conformal theories. In [17], Lam and Lui reported the quasi-conformal landmark registration (QCLR) algorithm for triangular meshes.

III. Contribution

Our proposed *TRIM* approach for accelerating image and video frame registration is advantageous in the following aspects:

1) The triangulation algorithm is fully automatic. The important features of the input image are well recorded in the resulting coarse triangulation.
2) The algorithm is fast and robust. The coarse triangulation of a typical high resolution image can be computed within seconds.
3) The registration of the original images can be simplified by a mapping of the coarse triangulation. The fine details are then restored with the aid of the coarse registration result.
4) Our proposed *TRIM* algorithm is particularly suitable for landmark-based registration as the landmark constraints can be easily included in the coarse triangulations. By contrast, for regular grid-based approaches, accurate landmark correspondences can only be achieved on a very dense grid domain representation.
5) Using our proposed approach, the problem scale of the image and video frame registration is significantly reduced. Our method can serve as a fast and accurate initialization for the state-of-the-art image registration algorithms.

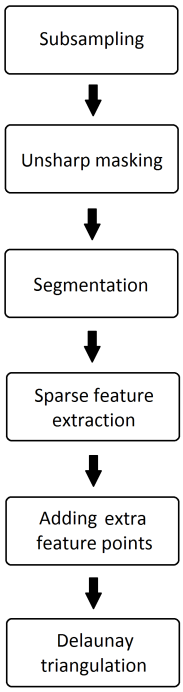

Fig. 1. The pipeline of our proposed *TRIM* algorithm for accelerating image registration via coarse triangulation.

IV. Proposed method

In this section, we describe our proposed *TRIM* image triangulation approach for efficient registration in details. The pipeline of our proposed framework is described in Figure 1.

A. Construction of coarse triangulation on images

Given two high resolution images I_1 and I_2, our goal is to compute a fast and accurate mapping $f : I_1 \to I_2$. Note that directly working on the high resolution images can be inefficient. To accelerate the computation, the first step is to construct a coarse triangular representation of the image I_1. In the following, we propose an efficient image triangulation scheme called *TRIM*. Our triangulation scheme is content-aware. Specifically, special objects and edges in the images are effectively captured by a segmentation step, and a suitable coarse triangulation is constructed with the preservation of these features. Our proposed *TRIM* method consists of 6 steps in total.

1) Subsampling the input image without affecting the triangulation quality: Denote the input image by I. To save the computational time for triangulating the input image I, one simple remedy is to reduce the problem size by performing certain subsampling on I. For ordinary images, subsampling unavoidably creates adverse effects on the image quality.

Nevertheless, it does not affect the quality of the coarse triangulation we aim to construct on images.

In our triangulation scheme, we construct triangulations based on the straight edges and special features on the images. Note that straight edges are preserved in all subsamplings of the images because of the linearity. Hence, our edge-based triangulation is not affected by the mentioned adverse effects. In other words, we can subsample high resolution images to a suitable size for enhancing the efficiency of the remaining steps for the construction of the triangulations. We denote the subsampled image by $\tilde{I}$.

2) Performing unsharp masking on the subsampled image: After obtaining the subsampled image $\tilde{I}$, we perform an unsharp masking on $\tilde{I}$ in order to preserve the edge information in the final triangulation. More specifically, we first transform the data format of the subsampled image $\tilde{I}$ to the CIELAB standard. Then, we apply the unsharp masking method in [26] on the intensity channel of the CIELAB representation of $\tilde{I}$. The unsharp masking procedure is briefly described as follows.

By an abuse of notation, we denote $\tilde{I}(x,y)$ and $\bar{I}(x,y)$ the intensities of the input subsampled image $\tilde{I}$ and the output image $\bar{I}$ respectively, and $G_\sigma(x,y)$ the Gaussian mean of the intensity of the pixel (x,y) with standard derivation σ. Specifically, $G_\sigma(x,y)$ is given by

$$G_\sigma(x,y) \triangleq \frac{1}{\sigma\sqrt{2\pi}} \int_{(u,v)\in\Omega} e^{-\frac{(u-x)^2+(v-y)^2}{2\sigma^2}}. \tag{1}$$

We perform an unsharp masking on the image using the following formula

$$\bar{I}(x,y) = \tilde{I}(x,y) - \lambda \begin{cases} G_\sigma * \tilde{I}(x,y) & \text{if } V_s(x,y) > \theta, \\ 0 & \text{if } V_s(x,y) < \theta, \end{cases} \tag{2}$$

where

$$V_s(x,y) \triangleq \sqrt{\frac{1}{Area(M_s)} \int_{(u,v)\in M_s} (\tilde{I}(u,v) - \tilde{I}_{mean}(x,y))^2} \tag{3}$$

and

$$\tilde{I}_{mean}(x,y) = \frac{1}{Area(M_s)} \int_{(u,v)\in M_s} \tilde{I}(u,v). \tag{4}$$

Here, M_s is the disk with center (x,y) and radius s. The effect of the unsharp masking is demonstrated in Figure 2. With the aid of this step, we can highlight the edge information in the resulting image $\bar{I}$ for the construction of the triangulation in the later steps. In our experiment, we choose $\lambda = 0.5,\ \sigma = 2,\ s = 2$, and $\theta = 0.5$.

3) Segmenting the image: After obtaining the image $\bar{I}$ upon unsharp masking, we perform a segmentation in this step in order to optimally locate the mesh vertices for computing the coarse triangulation. Mathematically, our segmentation problem is described as follows.

Suppose the image $\bar{I}$ has L intensity levels in each RGB channel. Denote i as a specific intensity level ($i.e.\ 0 \le i \le L-1$). Let C be a color channel of the image ($i.e.\ C \in \{R,G,B\}$), and let h_i^C denote the image histogram

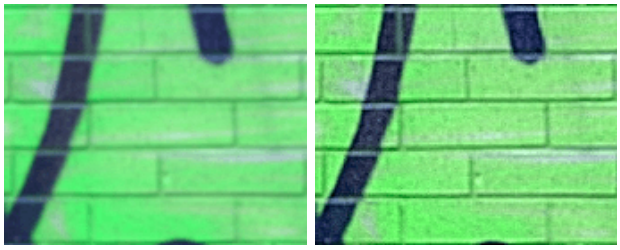

Fig. 2. An illustration of unsharp masking. Left: the input image. Right: the resulting image. The unsharp masking procedure helps preserving the edge information of the input image to ensure that the vertices in unclear edges can also be extracted.

for channel C, in other words, the number of pixels which correspond to its i-th intensity level.

Define $p_i^C \triangleq \frac{h_i^C}{N}$, where N represents the total number of pixels in the image $\bar{I}$. Then we have

$$\sum_{\substack{i=0,\\ C\in\{R,G,B\}}}^{L} p_i^C = 1 \quad \text{and} \quad \mu_T^C = \sum_{\substack{i=0,\\ C\in\{R,G,B\}}}^{L} i p_i^C. \tag{5}$$

Suppose that we want to compress the color space of the image $\bar{I}$ to l intensity levels. Equivalently, $\bar{I}$ is to be segmented into l regions $D_1^C, \cdots, D_l^C$ by the ordered threshold levels $x_j^C, j = 1, \cdots, l-1$. We define the best segmentation criterion to be maximizing the inter-region intensity-mean variance. More explicitly, we define the cost

$$\sigma^C \triangleq \sum_{\substack{j=1,\\ C\in\{R,G,B\}}}^{l} w_j^C (\mu_j^C - \mu_T^C)^2, \tag{6}$$

where the probability w_j^C of occurrence and the intensity-mean μ_j^C of the region D_j^C are respectively given by

$$w_j^C = \begin{cases} \sum\limits_{\substack{i=0,\\ C\in\{R,G,B\}}}^{t_j^C} p_i^C & \text{if } j = 1, \\ \sum\limits_{\substack{i=t_{j-1}^C+1,\\ C\in\{R,G,B\}}}^{t_j^C} p_i^C & \text{if } 1 < j < l, \\ \sum\limits_{\substack{i=t_j^C+1,\\ C\in\{R,G,B\}}}^{L-1} p_i^C & \text{if } j = l, \end{cases} \tag{7}$$

and

$$\mu_j^C = \begin{cases} \sum\limits_{\substack{i=0,\\ C\in\{R,G,B\}}}^{t_j^C} \frac{i p_i^C}{w_j^C} & \text{if } j = 1, \\ \sum\limits_{\substack{i=t_{j-1}^C+1,\\ C\in\{R,G,B\}}}^{t_j^C} \frac{i p_i^C}{w_j^C} & \text{if } 1 < j < l, \\ \sum\limits_{\substack{i=t_j^C+1,\\ C\in\{R,G,B\}}}^{L-1} \frac{i p_i^C}{w_j^C} & \text{if } j = l. \end{cases} \tag{8}$$

Hence, we maximize three objective functions of each RGB

Fig. 3. An illustration of the segmentation step for compressing the color space to achieve a sparse intensity representation. Left: the original image. Right: the segmentation result.

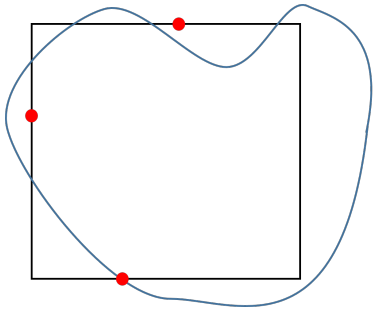

Fig. 4. An illustration of our sparse feature extraction scheme. The chosen sparse feature points are represented by the red dots. If the segment boundary does not intersect an edge, no point is selected. If the segment boundary intersects an edge at exactly one point, the point is selected as a feature point. If the segment boundary intersects an edge at multiple points, the centre of the points is selected as a feature point.

channel

$$\underset{1<x_1^C<\cdots<x_{l-1}^C<L}{\arg\max} \quad \sigma^C(\{x_j^C\}_{j=1}^{l-1}), \tag{9}$$

where $C \in \{R, G, B\}$. Our goal is to find a set of $\mathbf{x} = \{x_j^C\}_{j=1}^{l-1}$ such that above function is maximized for each RGB channel.

To solve the aforementioned segmentation optimization problem, we apply the Particle Swarm Optimization (PSO) segmentation algorithm [9] on the image $\bar{I}$. The PSO method is used in this segmentation optimization problem for reducing the chance of trapping in local optimums.

An illustration of the segmentation step is provided in Figure 3. After performing the segmentation, we extract the boundaries of the segments. Then, we can obtain a number of large patches of area in each of which the intensity information is almost the same. They provide us with a reasonable edge base for constructing a coarse triangulation in later steps.

4) Sparse feature extraction on the segment boundaries: After computing the segment boundaries $\mathcal{B}$ on the image $\bar{I}$, we aim to extract sparse feature points on $\mathcal{B}$ in this step. For the final triangulation, it is desirable that the edges of the triangles are as close as possible to the segment boundaries $\mathcal{B}$, so as to preserve the geometric features of the original image I. Also, to improve the efficiency for the computations on the triangulation, the triangulation should be much coarser than the original image. To achieve the mentioned goals, we consider extracting sparse features on the segment boundaries $\mathcal{B}$ and use them as the vertices of the ultimate triangulated mesh.

Consider a rectangular grid table G on the image $\bar{I}$. Apparently, the grid table G intersects the segment boundaries $\mathcal{B}$ at a number of points. Denote $\mathcal{P}$ as our desired set of sparse features. Conceptually, $\mathcal{P}$ is made up of the set of points at which $\mathcal{B}$ intersect the grid G, with certain exceptions.

In order to further reduce the number of feature points for a coarse triangulation, we propose a merging procedure for close points. Specifically, let $g_{i,j}$ be the vertex of the grid G at the i-th row and the j-th column. We denote $\mathcal{P}_{i,j}^1$ and $\mathcal{P}_{i,j}^2$ respectively as the set of points at which $\mathcal{B}$ intersect the line segment $\overline{g_{i,j}g_{i,j+1}}$ and the line segment $\overline{g_{i,j}g_{i+1,j}}$.

There are 3 possible cases for $\mathcal{P}_{i,j}^k$:

(i) If $|\mathcal{P}_{i,j}^k| = 0$, then there is no intersection point between the line segment and $\mathcal{B}$ and hence we can neglect it.

(ii) If $|\mathcal{P}_{i,j}^k| = 1$, then there is exactly one intersection point $p_{i,j}^k$ between the line segment and $\mathcal{B}$. We include this intersection point $p_{i,j}^k$ in our desired set of sparse features $\mathcal{P}$.

(iii) If $|\mathcal{P}_{i,j}^k| > 1$, then there are multiple intersection points between the line segment and $\mathcal{B}$. Since these multiple intersection points lie on the same line segment, it implies that they are sufficiently close to each other. In other words, the information they contain about the segment boundaries $\mathcal{B}$ is highly similar and redundant. Therefore, we consider merging these multiple points as one point.

More explicitly, for the third case, we compute the centre $m_{i,j}^k$ of the points in $\mathcal{P}_{i,j}^k$ by

$$m_{i,j}^k = mean_{\{p|p\in\mathcal{P}_{i,j}^k\}}p. \tag{10}$$

The merged point $m_{i,j}^k$ is then considered as a desired feature point. In summary, our desired set of sparse features is given by

$$\mathcal{P} = \bigcup_i \bigcup_j \{p_{i,j}^1, p_{i,j}^2, m_{i,j}^1, m_{i,j}^2\}. \tag{11}$$

An illustration of the sparse feature extraction scheme is given in Figure 4. However, one important problem in this scheme is to determine a suitable size of the grid G so that the sparse feature points are optimally computed. Note that to preserve the regularity of the extracted sparse features, it is desirable that the elements of the grid G are close to perfect squares. Also, to capture the important features as complete as possible, the elements of G should be small enough. Mathematically, the problem can be formulated as follows.

Denote w as the width of the image $\bar{I}$, h as the height of the image $\bar{I}$, w' as the number of columns in G, h' as the number of rows in G, l_w as the horizontal length of every element of G, and l_h as the vertical length of every element of G. We further denote p as the percentage of grid edges in G which intersect the segment boundaries $\mathcal{B}$, and n as the desired number of the sparse feature points. Given the two

inputs p and n which respectively correspond to the desired sparse ratio and the desired number of feature points, to find a suitable grid size of G, we aim to minimize the cost function

$$c(l_w, l_h) = |l_w - l_h|^2 \tag{12}$$

subject to

(i)
$$h = h' l_h, \tag{13}$$

(ii)
$$w = w' l_w, \tag{14}$$

(iii)
$$p(w' + h' + 2w'h') = n. \tag{15}$$

Here, the first and the second constraint respectively correspond to the horizontal and vertical dimensions of the grid G, and the third constraint corresponds to the total number of intersection points. To justify Equation (15), note that

$$\begin{aligned} &\text{Total number of line segments} \\ &= \text{Total number of horizontal line segments} \\ &\quad + \text{Total number of vertical line segments} \\ &= h'(w'+1) + w'(h'+1) \\ &= w' + h' + 2w'h'. \end{aligned} \tag{16}$$

Note that this minimization problem is nonlinear. To simplify the computation, we assume that w', h' are very large, that is, the grid G is sufficiently dense. Then, from Equation (15), we have

$$\begin{aligned} \frac{p}{n} &= \frac{1}{w' + h' + 2w'h'} \\ &\approx \frac{1}{2w'h'} \\ &= \frac{1}{2\left(\frac{w}{l_w}\right)\left(\frac{h}{l_h}\right)} \\ &= \frac{l_w l_h}{2wh}. \end{aligned} \tag{17}$$

By further assuming that the grid G is sufficiently close to a square grid, we have $l_w \approx l_h$. Then, it follows that

$$\frac{p}{n} \approx \frac{l_w^2}{2wh} \tag{18}$$

and hence

$$l_w \approx \sqrt{\frac{2pwh}{n}}. \tag{19}$$

Similarly,

$$l_h \approx \sqrt{\frac{2pwh}{n}}. \tag{20}$$

To satisfy the integral constraints for w' and h', we make use of the above approximations and set

$$h' = h'_0 := \left\lfloor \frac{h}{\sqrt{\frac{2pwh}{n}}} \right\rfloor = \left\lfloor \sqrt{\frac{nh}{2pw}} \right\rfloor. \tag{21}$$

Similarly, we set

$$w' = w'_0 := \left\lfloor \frac{w}{\sqrt{\frac{2pwh}{n}}} \right\rfloor = \left\lfloor \sqrt{\frac{nw}{2ph}} \right\rfloor. \tag{22}$$

Finally, we take

$$l_h = \frac{h}{h'_0} \tag{23}$$

and

$$l_w = \frac{w}{w'_0}. \tag{24}$$

To summarize, with the abovementioned strategy for the feature point extraction, we obtain a set of sparse feature points which approximates the segment boundaries $\mathcal{B}$. Specifically, given the inputs p and n, the rectangular grid G we introduce leads to approximately n regularly-extracted sparse feature points. An illustration of the sparse feature extraction scheme is shown in Figure 5 (left). In our experiments, p is set to be 0.2. A denser triangulated representation can be achieved by increasing the value of p.

5) Adding landmark points to the vertex set of the desired coarse triangulation: This step is only required when our *TRIM* algorithm is used for landmark-constrained registration. For accurate landmark-constrained registration, it is desirable to include the landmark points in the vertex set of the coarse representations of the input image I. One of the most important features of our coarse triangulation approach is that it allows registration with exact landmark constraints on a coarse triangular representation. By contrast, the regular grid-based registration can only be achieved on very dense rectangular grid domains in order to reduce the numerical errors.

With the abovementioned advantage of our approach, we can freely add a set of landmark points $\mathcal{P}_{LM}$ to the set of sparse features $\mathcal{P}$ extracted by the previous procedure. In other words, the landmark points are now considered as a part of our coarse triangulation vertices:

$$\mathcal{P} = \bigcup_i \bigcup_j \{p^1_{i,j}, p^2_{i,j}, m^1_{i,j}, m^2_{i,j}\} \cup \mathcal{P}_{LM}. \tag{25}$$

Then, the landmark-constrained registration of images can be computed by the existing feature-matching techniques for triangular meshes. The existing feature detection approaches such as [12] and [20] can be applied for obtaining the landmark points.

6) Computing a Delaunay triangulation: In the final step, we construct a triangulation based on the set $\mathcal{P}$ of feature points. Among all triangulation schemes, the Delaunay triangulation method is chosen since the triangles created by the Delaunay triangulations are more regular. More specifically, if α and β are two angles opposite to a common edge in a Delaunay triangulation, then they must satisfy the inequality

$$\alpha + \beta \leq \pi. \tag{26}$$

In other words, Delaunay triangulations avoid the formation of sharp and irregular triangles. Note that the regularity does

not only enhance the visual quality of the resulting triangulation but also lead to a more stable approximation of the derivatives on the triangles when applying various registration schemes. Therefore, we compute a Delaunay triangulation on the set $\mathcal{P}$ of feature points for achieving the ultimate triangulation $\mathcal{T}$. An illustration of the construction of the Delaunay triangulations is shown in Figure 5.

These 6 steps complete our *TRIM* algorithm as summarized in Algorithm 1.

Algorithm 1: Our proposed *TRIM* algorithm for triangulating an image.

Input: An image I, the desired number of image intensity levels l for segmentation, the desired number of feature points n, the sparse ratio p.

Output: A coarse triangulation $\mathcal{T}$ that captures the main features of the image.

1 Subsample the input image I to a suitable size and denote the result by $\tilde{I}$;
2 Apply an unsharp masking on the subsampled image $\tilde{I}$ and denote the result by $\bar{I}$;
3 Apply the PSO segmentation for compressing the color space of $\bar{I}$ to l intensity levels, and extract boundaries $\mathcal{B}$ of the segments;
4 Extract a set of sparse feature points $\mathcal{P}$ from the segment boundaries $\mathcal{B}$ based on the parameters n and p;
5 Add a set of extra landmark points $\mathcal{P}_{LM}$ to $\mathcal{P}$ if necessary;
6 Compute a Delaunay triangulation $\mathcal{T}$ on the sparse feature points $\mathcal{P}$.

It is noteworthy that our proposed *TRIM* algorithm significantly trims down high resolution images without distorting their important geometric features. Experimental results are shown in Section V to demonstrate the effectiveness of the *TRIM* algorithm.

B. Simplification of the registration using the coarse triangulation

With the above triangulation algorithm for images, we can simplify the image registration problem as a mapping problem of triangulated surfaces. Many conventional image registration approaches are hindered by the long computational time and the accuracy of the initial maps. With the new strategy, it is easy to obtain a highly efficient and reasonably accurate registration of images. Our registration result can serve as a high quality initial map for various algorithms.

In this work, we apply our proposed *TRIM* algorithm for landmark-aligned quasi-conformal image registration. Ideally, conformal registration are desired as conformal mappings preserve angles and hence the local geometry of the images. However, with the presence of landmark constraints, conformal mappings may not exist. We turn to consider quasi-conformal mappings, a type of mappings which is closely related to the conformal mappings. Mathematically, a *quasi-conformal mapping* $f : \mathbb{C} \to \mathbb{C}$ satisfies the Beltrami equation

$$\frac{\partial f}{\partial \bar{z}} = \mu(z)\frac{\partial f}{\partial z} \tag{27}$$

with μ is a complex-valued function with sup norm less than 1. μ is called the *Beltrami coefficient* of f. Intuitively, a conformal mapping maps infinitesimal circles to infinitesimal circles, while a quasi-conformal mapping maps infinitesimal circles to infinitesimal ellipses (see Figure 6). Readers are referred to [7] for more details.

In [17], Lam and Lui proposed the quasi-conformal landmark registration (QCLR) algorithm for triangular meshes. In this work, we apply the QCLR algorithm on our coarse triangulations of images. More explicitly, to compute a registration mapping $f : I_1 \to I_2$ between two images I_1 and I_2 with prescribed point correspondences

$$p_i \longleftrightarrow q_i, i = 1, 2, \cdots, n, \tag{28}$$

we first apply our proposed *TRIM* algorithm and obtain a coarse triangulation $\mathcal{T}_1$ on I_1. Here, we include the feature points $\{p_i\}_{i=1}^n$ in the generation of the coarse triangulation, as described in the fifth step of the *TRIM* algorithm. Then, instead of directly computing f, we can solve for a map $\tilde{f} : \mathcal{T}_1 \to I_2$. Since the problem size is significantly reduced under the coarse triangulation, the computation for $\tilde{f}$ is much more efficient than that for f.

The QCLR algorithm [17] aims to compute the desired quasi-conformal mapping $\tilde{f}$ by minimizing the energy functional

$$E_{LM}(\nu) = \int_{\mathcal{T}_1} |\nabla\nu|^2 + \alpha \int_{\mathcal{T}_1} |\nu|^2 \tag{29}$$

subject to

(i) $\tilde{f}(p_i) = q_i$ for all $i = 1, 2, \cdots, n$,
(ii) $\|\nu\|_\infty < 1$, and
(iii) $\nu = \mu(\tilde{f})$.

To solve the above minimization problem (29), the QCLR algorithm makes use of the penalty splitting method and minimizes

$$E_{LM}^{split}(\nu, \tilde{f}) = \int_{\mathcal{T}_1} |\nabla\nu|^2 + \alpha \int_{\mathcal{T}_1} |\nu|^2 + \rho \int_{\mathcal{T}_1} |\nu - \mu(\tilde{f})|^2 \tag{30}$$

subject to

(i) $\tilde{f}(p_i) = q_i$ for all $i = 1, 2, \cdots, n$ and
(ii) $\|\nu\|_\infty < 1$.

The QCLR algorithm then alternately minimizes the energy E_{LM}^{split} over one of ν and $\tilde{f}$ while fixing the other one.

Specifically, for computing $\tilde{f}_n$ while fixing ν_n and the landmark constraints, the QCLR algorithm applies the Linear Beltrami Solver proved by Lui et al.[24]. On the other hand, for computing ν_{n+1} while fixing $\tilde{f}_n$, by considering the Euler-Lagrange equation, it suffices to solve

$$(-\Delta + 2\alpha I + 2\rho I)\nu_{n+1} = 2\rho\mu(\tilde{f}_n). \tag{31}$$

From ν_{n+1}, one can compute the associated quasi-conformal mapping $\tilde{f}_{n+1}$. However, note that $\tilde{f}_{n+1}$ may not satisfy the hard landmark constraints 28 anymore. To enforce

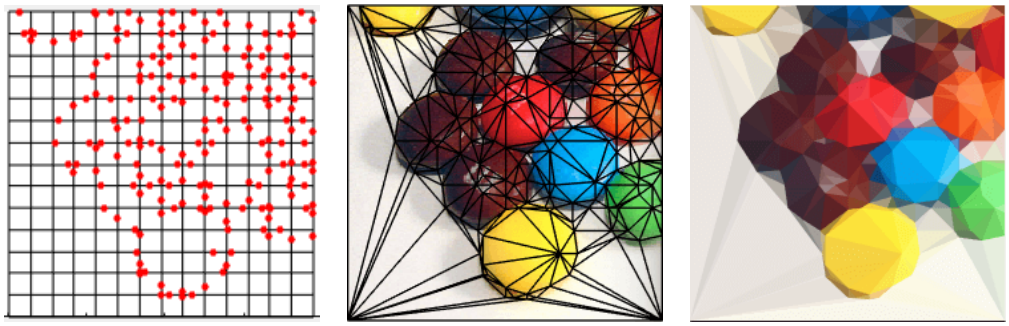

Fig. 5. An illustration of extracting the vertices and computing a Delaunay triangulation. Left: the points obtained by the feature extraction step from Figure 3. Middle: a Delaunay triangulation generated on the feature points. Right: the triangulation with a color approximated on each triangle.

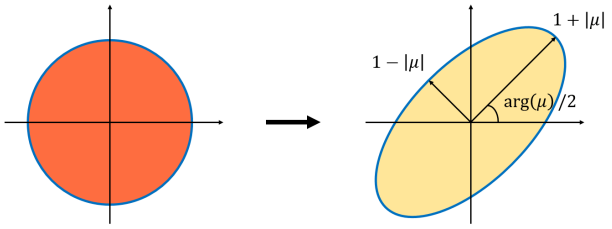

Fig. 6. An illustration of quasi-conformal mappings. The maximal magnification and shrinkage are determined by the Beltrami coefficient μ of the mappings.

the landmark constraints, instead of directly using $\tilde{f}_{n+1}$ as the updated result, the QCLR algorithm updates ν_{n+1} by

$$\nu_{n+1} \leftarrow \nu_{n+1} + t(\mu(\tilde{f}_{n+1}) - \nu_{n+1}) \tag{32}$$

for some small t. By repeating the abovementioned procedures, we achieve a landmark-constrained quasi-conformal mapping $\tilde{f}$. For more details of the QCLR algorithm, readers are referred to [17].

After computing the quasi-conformal mapping $\tilde{f}$ on the coarse triangulation, we apply an interpolation to retrieve the fine details of the registration. Since the triangulations created by our proposed *TRIM* algorithm preserves the important geometric features and prominent straight lines of the input image, the details of the registration results can be accurately interpolated. Moreover, since the coarse triangulation largely simplifies the input image and reduces the problem size, the computation is largely accelerated.

The registration procedure is summarized in Algorithm 2. Experimental results are illustrated in Section V to demonstrate the significance of our coarse triangulation in the registration scheme.

V. Experimental results

In this section, we demonstrate the effectiveness of our proposed triangulation scheme. The algorithms are implemented using MATLAB. For solving the mentioned linear systems, the backslash operator (\) in MATLAB is used. The test images are courtesy of the RetargetMe dataset [27]. The bird image is courtesy of the first author. All experiments are performed on a PC with an Intel(R) Core(TM) i7-4500U CPU @1.80 GHz processor and 8.00 GB RAM.

Algorithm 2: Feature-based registration via our proposed *TRIM* algorithm.

Input: Two images or video frames I_1, I_2 to be registered, with the prescribed feature correspondences.

Output: A feature-matching registration mapping $f : I_1 \to I_2$.

1. Compute a coarse triangulation $\mathcal{T}_1$ of I_1 using our proposed *TRIM* algorithm (Algorithm 1). Here, we include the prescribed feature points on I_1 in the generation of the coarse triangulation $\mathcal{T}_1$;
2. Select landmark correspondences of the coarse triangulation $\mathcal{T}_1$ and the target image I_2. Denote the landmark points on $\mathcal{T}_1$ and I_2 by $\{p_i\}_{i=1}^n$ and $\{q_i\}_{i=1}^n$ correspondingly;
3. Compute a landmark based quasi-conformal mapping $\tilde{f} : \mathcal{T}_1 \to \mathbb{C}$ by the QCLR algorithm in [17];
4. Obtain f by $\tilde{f}$ with a bilinear interpolation between $\mathcal{T}_j$ and I_j.

A. The performance of our proposed TRIM triangulation scheme

In this subsection, we demonstrate the effectiveness of our triangulation scheme by various examples.

Our proposed algorithm is highly content-aware. Specifically, regions with high similarities or changes in color on an image can be easily recognized. As a result, the triangulations created faithfully preserve the important features by a combination of coarse triangles with different sizes. Some of our triangulation results are illustrated in Figure 7. For better visualizations, we color the resulting triangulations by mean of the original colors of corresponding patches. In Figure 8, we apply our *TRIM* algorithm on a bee image. It can be observed that the regions of the green background can be effectively represented by coarser triangulations, while the region of the bee and flowers with apparent color differences is well detected and represented by a denser triangulation. Figure 9 shows another example of our triangulation result. The butterfly and the flowers are well represented in our triangulation result. The above examples demonstrate the effectiveness of our triangulation scheme for representing images in a simplified

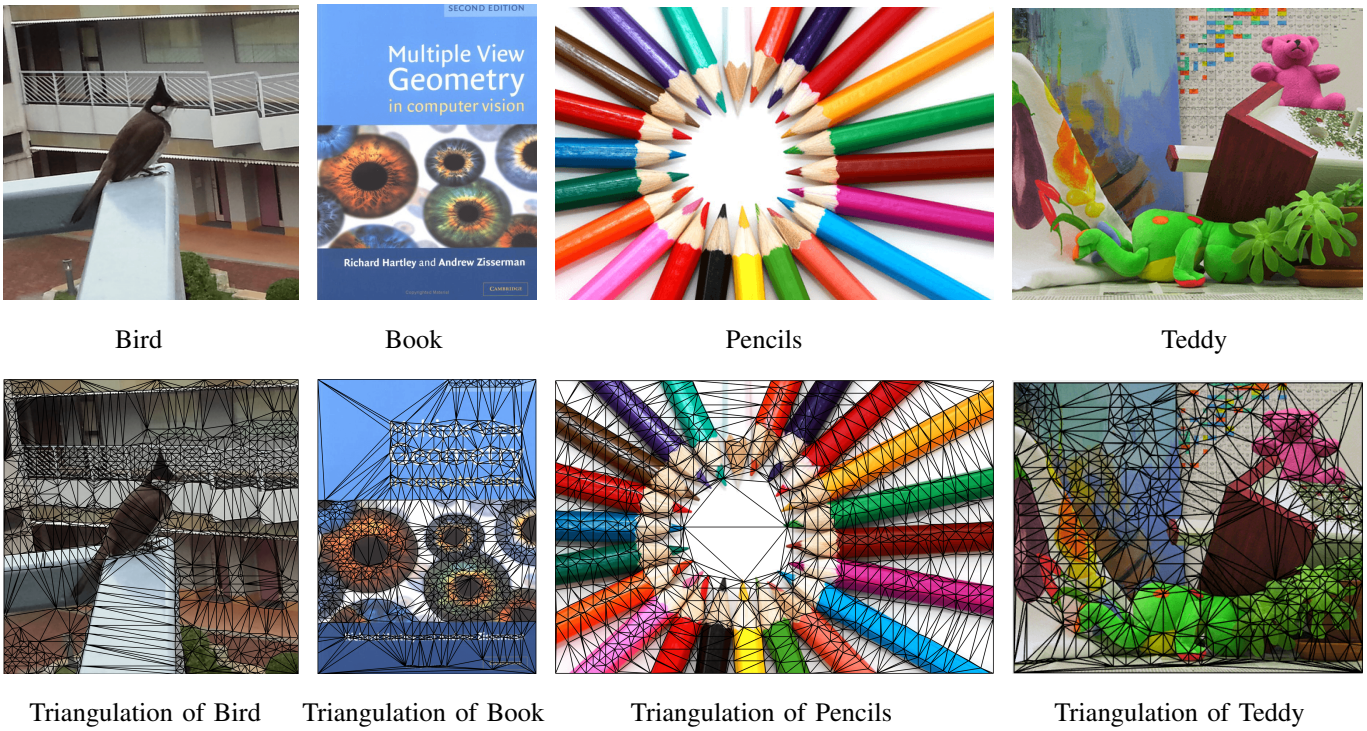

Fig. 7. Several images and the triangulations created by our *TRIM* algorithm. Top: the input images. Bottom: the resulting triangulations. The key features of the original images are well represented in our triangulations, and the regions with similar color can be represented by coarse triangulations.

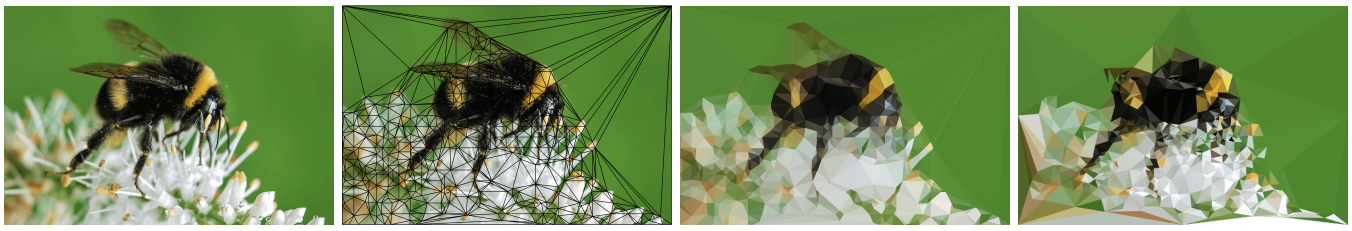

Fig. 8. A bee image and the triangulations created by our *TRIM* algorithm and DMesh [6]. Left: The input image. Middle left: The coarse triangulation created by *TRIM*. Middle right: Our *TRIM* coarse triangulation with a color approximated on each triangle. Right: The triangulation by DMesh [6].

but accurate way. Some more triangulation examples created by our *TRIM* algorithm are shown in Figure 10. Figure 11 shows some triangulation examples for noisy images. It can be observed that our *TRIM* algorithm can effectively compute content-aware coarse triangulations even for noisy images.

We have compared our algorithm with the DMesh triangulator [6] in Figure 8, Figure 9 and Figure 10. It can be observed that our triangulation scheme outperforms DMesh [6] in terms of the triangulation quality. Our results can better capture the important features of the images. Also, the results by DMesh [6] may contain unwanted holes while our triangulation results are always perfect rectangles. The comparisons reflect the advantage of our coarse triangulation scheme.

Then, we evaluate the efficiency of our triangulation scheme for various images. Table I shows the detailed statistics. The relationship between the target coarse triangulation size and the computational time is illustrated in Figure 12. Even for high resolution images, the computational time for the triangulation is only around 10 seconds. It is noteworthy that our *TRIM* algorithm significantly compresses the high resolution images as coarse triangulations with only several thousand triangles.

It is noteworthy that the combination of the steps in our *TRIM* algorithm is important for achieving a coarse triangulation. More specifically, if certain steps in our algorithm are removed, the triangulation result will become unsatisfactory. Figure 13 shows two examples of triangulations created by our entire *TRIM* algorithm and by our algorithm with the segmentation step excluded. It can be easily observed that without the segmentation step, the resulting triangulations are extremely dense and hence undesirable for simplifying further computations. By contrast, the number of triangles produced by our entire *TRIM* algorithm is significantly reduced. The examples highlight the importance of our proposed combination of steps in the *TRIM* algorithm for content-aware coarse triangulation.

Fig. 9. An butterfly image and the triangulations created by our *TRIM* algorithm and DMesh [6]. Left: The input image. Middle left: The coarse triangulation created by *TRIM*. Middle right: Our *TRIM* coarse triangulation with a color approximated on each triangle. Right: The triangulation by DMesh [6].

Fig. 10. Two more examples created by our *TRIM* algorithm and Dmesh [6]. Our coarse triangulations capture the important features and closely resemble the original images. Left: The input image. Middle: The coarse triangulation created by *TRIM*. Right: The triangulation by DMesh [6].

Image	Size	Triangulation time (s)	# of triangles	Compression rate
Surfer	846 × 421	5.78	1043	0.1536%
Helicopter	720 × 405	5.78	1129	0.1989%
Bee	640 × 425	7.13	1075	0.2029%
Bird	1224 × 1224	7.04	1287	0.0859%
Butterfly	1024 × 700	8.00	1720	0.1232%
Book	601 × 809	8.38	1629	0.3350%
Baseball	410 × 399	7.85	2315	0.7201%
Bear	450 × 375	7.48	2873	0.8652%
Pencil	615 × 410	8.93	2633	0.5838%
Tiger	2560 × 1600	13.91	3105	0.0414%
Eagle	600 × 402	13.27	1952	0.4299%

TABLE I
PERFORMANCE OF OUR *TRIM* ALGORITHM. HERE, THE COMPRESSION RATE IS DEFINED BY $\frac{\#\text{ OF TRIANGLE NODES}}{\#\text{ OF PIXELS}} \times 100\%$.

B. The improvement in efficiency of image registration by our TRIM *algorithm*

In this subsection, we demonstrate the effectiveness of our proposed triangulation-based method for landmark-based image registration. In our experiments, the feature points on the images are extracted using the algorithm by Harris and Stephens [12] as landmark constraints. For simplifying the image registration problems, one conventional approach is to make use of coarse regular grids followed by interpolation. It is natural to ask whether our proposed coarse

Fig. 11. Two triangulation examples by our *TRIM* algorithm for noisy images. Left: The noise-free images. Middle left: The triangulations computed by *TRIM* based on the noise-free images. Middle right: The noisy images. Right: The triangulations computed by *TRIM* based on the noisy images. It can be observed that the important features of the images are preserved even for noisy images.

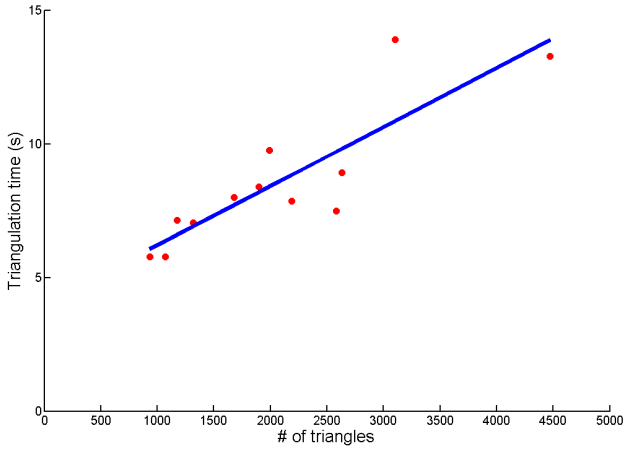

Fig. 12. The relationship of the desired coarse triangulation size and the computational time of our proposed *TRIM* algorithm.

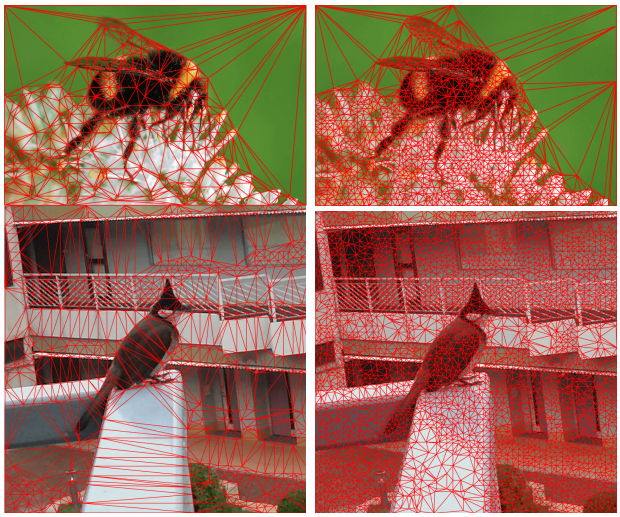

Fig. 13. The triangulations created by our entire *TRIM* algorithm (left) and by the algorithm without the segmentation step (Right). It can be observed that the segmentation step is crucial for achieving a coarse triangulation. Number of triangles produced: 923 (top left), 3612 (top right), 1496 (bottom left), 8685 (bottom right).

triangulation-based method produces better results. In Figure 14, we consider a stereo registration problem of two scenes. With the prescribed feature correspondences, we compute the feature-endowed stereo registration via the conventional grid-based approach, the DMesh triangulation approach [6] and our proposed *TRIM* method. For the grid-based approach and the DMesh triangulation approach [6], we take the mesh vertices nearest to the prescribed feature points on the source image as source landmarks. For our proposed *TRIM* method, as the landmark vertices are automatically embedded in the content-aware coarse triangulation, the source landmarks are exactly the feature points detected by the method in [12].

It can be observed that our triangulation-based approach produces a much more natural and accurate registration result when compared with both the grid-based approach and the DMesh triangulation approach. In particular, sharp features such as edges are well preserved using our proposed method. By contrast, the edges are seriously distorted in the other two methods. In addition, the geometry of the background in the scenes are well retained via our *TRIM* method but not the other two methods. The higher accuracy of the registration result by our approach can also be visualized by the intensity difference plots. Our triangulation-based approach results in an intensity difference plot with more dark regions than the other two approaches. The advantage of our method over the other

two methods is attributed to the geometry preserving feature of our *TRIM* algorithm, in the sense that the triangulations created by *TRIM* are more able to fit into complex features and have more flexibilities in size than regular grids. Also, the triangulations created by DMesh [6] do not capture the geometric features and hence the registration results are unsatisfactory. They reflect the significance of our content-aware *TRIM* triangulation scheme in computing image registration. Another example is illustrated in Figure 15. Again, it can be easily observed that our proposed *TRIM* triangulation approach leads to a more accurate registration result.

To highlight the improvement in the efficiency by our proposed *TRIM* algorithm, Table II records the computational time and the error of the registration via the conventional grid-based approach and our *TRIM* triangulation-based approach. It is noteworthy that our proposed coarse triangulation-based method significantly reduces the computational time by over 85% on average when compared with the traditional regular grid-based approach. To quantitatively assess the quality of the registration results, we define the matching accuracy by

$$\frac{\text{\# pixels s.t.} \|\text{final intensity - original intensity}\|_1 < \epsilon}{\text{Total \# of pixels}} \times 100\%. \tag{33}$$

The threshold ϵ is set to be 0.2 in our experiments. Our triangulation-based method produces registration results with the matching accuracy higher than that of the regular grid-based method by 3% on average. The experimental results reflect the advantages of our *TRIM* content-aware coarse triangulations for image registration.

VI. Conclusion and future work

In this paper, we have established a new framework for accelerating image registration. Using our proposed *TRIM* algorithm, a content-aware coarse triangulation is built on a high resolution image. Then, we can efficiently compute a landmark-based registration using the coarse triangulation. From the coarse registration result, we can obtain the desired fine registration result. Our proposed method is advantageous for a large variety of registration applications with a significant improvement of the computational efficiency and registration accuracy. Hence, our proposed method can serve as an effective initialization for various registration algorithms. In the future, we aim to extend our proposed *TRIM* algorithm in the following two directions.

1) n-dimensional registration via TRIM*:* Our work can be naturally extended for higher dimensional registration problems. For accelerating n-dimensional volumetric registration, one can consider constructing a coarse representation using n-simplices. Analogous to our 2-dimensional *TRIM* algorithm, the n-dimensional coarse representation should also result in a significant improvement of the efficiency for n-dimensional registration problems.

2) TRIM *image compression format:* Recall that in our proposed *TRIM* algorithm, there are two important parameters, namely, the number of intensity threshold levels l in the image segmentation step and the sparse ratio p for controlling the fineness of the triangular representation. By increasing the values of these two parameters, an image intensity representation becomes more accurate. Hence, given a compression error threshold, we aim to develop an iterative *TRIM* scheme for continuously increasing the two values until the intensity difference between the compressed image and the original image is smaller than the prescribed error threshold. This provides us with a new image compression format using *TRIM*. Since the *TRIM* compression format only consists of the coarse triangular mesh vertices and the corresponding colors, the compression size is much smaller than that of the existing image compression formats.

References

[1] F. L. Bookstein, *The measurement of biological shape and shape change*. Springer-Verlag: Lecture Notes in Biomathematics, Volume 24, pp. 1–191, 1978.

[2] F. L. Bookstein, *Morphometric tools for landmark data*. Cambridge University Press, Cambridge, 1991.

[3] F. L. Bookstein, *Linear methods for nonlinear maps: Procrustes fits, thin-plate splines, and the biometric analysis of shape variability*. Brain Warping, Academic Press, London, pp. 157–181, 1999.

[4] P. T. Choi, K. C. Lam, and L. M. Lui, *FLASH: Fast landmark aligned spherical harmonic parameterization for genus-0 closed brain surfaces*. SIAM Journal on Imaging Sciences, Volume 8, Issue 1, pp. 67–94, 2015.

[5] W. R. Crum, T. Hartkens, and D. L. G. Hill, *Non-rigid image registration: theory and practice*. The British Journal of Radiology, Volume 77, pp. 140–153, 2004.

[6] D. Y. H. Yun, *DMesh triangulation image generator*. http://dmesh.thedofl.com/

[7] F. Gardiner and N. Lakic, *Quasiconformal Teichmüller theory*. Mathematical Surveys and Monographs, Volume 76, American Mathematics Society, 2000.

[8] J. C. Gee, D. R. Haynor, M. Reivich, and R. Bajcsy, *Finite element approach to warping of brain images*. Proceedings of SPIE, pp. 327–337, 1994.

[9] P. Ghamisi, M. S. Couceiro, J. A. Benediktsson, and N. M. F. Ferreira, *An efficient method for segmentation of images based on fractional calculus and natural selection*. Expert Systems with Applications, Volume 39, Issue 16, pp. 12407–12417, 2012.

[10] J. Glaunès, M. Vaillant, and M. I. Miller, *Landmark matching via large deformation diffeomorphisms on the sphere*. Journal of mathematical imaging and vision, Volume 20, Issue 1, pp. 179–200, 2004.

[11] J. Glaunès, A. Qiu, M. I. Miller, and L. Younes, *Large deformation diffeomorphic metric curve mapping*. International journal of computer vision, Volume 80, Issue 3, pp. 317–336, 2008.

[12] C. Harris and M. Stephens, *A combined corner and edge detector*. Proceedings of the 4th Alvey Vision Conference. pp. 147–151, 1988.

[13] H. J. Johnson, G. E. Christensen, *Consistent landmark and intensity-based image registration*. IEEE Transactions on Medical Imaging, Volume 21, Issue 5, pp. 450–461, 2002.

[14] S. C. Joshi and M. I. Miller, *Landmark matching via large deformation diffeomorphisms*. IEEE Transactions on Image Processing, Volume 9, Issue 8, pp. 1357–1370, 2000.

[15] P. Kaufmann, O. Wang, A. Sorkine-Hornung, O. Sorkine-Hornung, A. Smolic, and M. Gross, *Finite Element Image Warping*. Computer Graphics Forum, Volume 32, Issue 2pt1, pp. 31–39, May 2013.

[16] A. Klein, J. Andersson, B.A. Ardekani, J. Ashburner, B. Avants, M.-C. Chiang, G. E. Christensen, D. L. Collins, J. Gee, P. Hellier, J. H. Song, M. Jenkinson, C. Lepage, D.Rueckert, P. Thompson, T. Vercauteren, R. P. Woods, J. J. Mann, and R. V. Parsey, *Evaluation of 14 nonlinear deformation algorithms applied to human brain MRI registration*. NeuroImage, Volume 46, Issue 3, pp. 786–802, 2009.

[17] K. C. Lam and L. M. Lui, *Landmark and intensity based registration with large deformations via quasi-conformal maps*. SIAM Journal on Imaging Sciences, Volume 7, Issue 4, pp. 2364–2392, 2014.

[18] B. Lehner, G. Umlauf, B. Hamann, *Image compression using data-dependent triangulations*. International Symposium on Visualization and Computer Graphics, pp. 351–362, 2007.

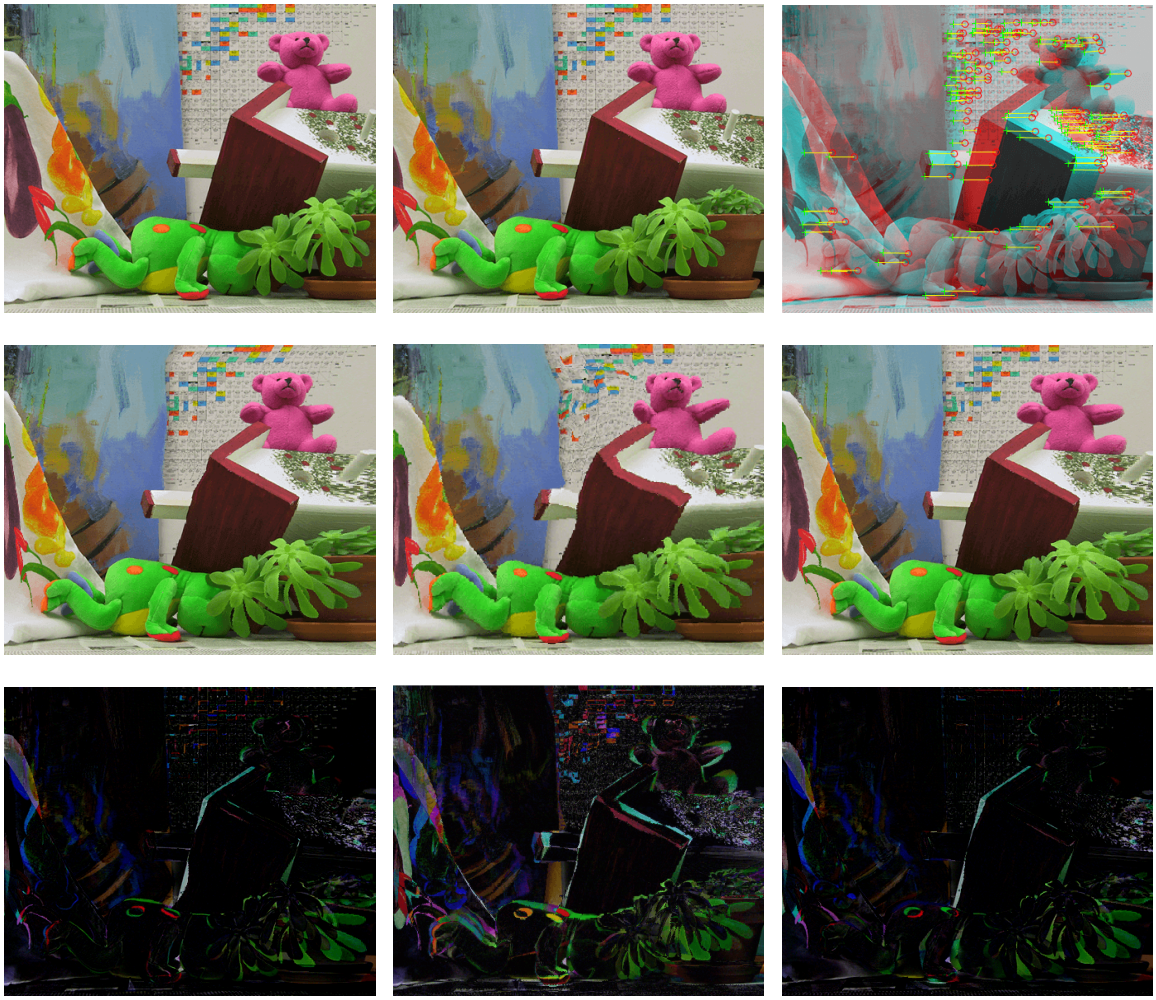

Fig. 14. Stereo landmark registration using different algorithms. Top left: The source image. Top middle: The target image. Top Right: The prescribed feature correspondences. Middle left: The registration result by the dense grid-based approach (4 pixels per grid). Middle: The registration result via DMesh [6]. Middle right: The registration result by our proposed coarse triangulation-based method. Bottom left: The intensity difference after the registration by the dense grid-based approach. Bottom middle: The intensity difference after the registration via DMesh [6]. Bottom right: The intensity difference after the registration by our proposed coarse triangulation-based method. Because of the greater flexibility of our triangulation scheme, the accuracy of registration by our method is higher than that of the dense grid-based approach.

Images	Size	Registration				Time saving rate
		Via regular grids		Via *TRIM*		
		Time (s)	Matching accuracy (%)	Time (s)	Matching accuracy (%)	
Bear	450 × 375	102.3	59.5	13.8	70.7	13.4897%
Cone	450 × 375	108.7	51.3	28.2	61.2	25.9430%
Cloth	1252 × 1110	931.0	70.7	36.0	75.4	3.8668%
Book	1390 × 1110	1204.5	59.0	51.0	63.0	4.2341%
Baby	1390 × 1110	94.3	62.3	11.0	62.3	11.6649%

TABLE II
THE PERFORMANCE OF FEATURE-BASED IMAGE REGISTRATION VIA OUR PROPOSED *TRIM* COARSE TRIANGULATION METHOD AND THE ORDINARY COARSE GRIDS. HERE, THE TIME SAVING RATE IS DEFINED BY $\frac{\text{REGISTRATION TIME VIA } TRIM}{\text{REGISTRATION TIME VIA REGULAR GRIDS}} \times 100\%$.

[19] B. Lehner, G. Umlauf, B. Hamann, *Video compression using data-dependent triangulations*. Computer Graphics and Visualization, pp. 244–248, 2008.

[20] D. Lowe, *Distinctive image features from scale-invariant keypoints*. International Journal of Computer Vision, Volume 60, Issue 2, pp. 91–110, 2004.

[21] L. M. Lui, Y. Wang, T. F. Chan, and P. M. Thompson, *Landmark constrained genus zero surface conformal mapping and its application to brain mapping research*. Applied Numerical Mathematics, Volume 57, Issue 5–7, pp. 847–858, 2007.

[22] L. M. Lui, S. Thiruvenkadam, Y. Wang, P. M. Thompson, and T. F. Chan, *Optimized conformal surface registration with shape-based landmark*

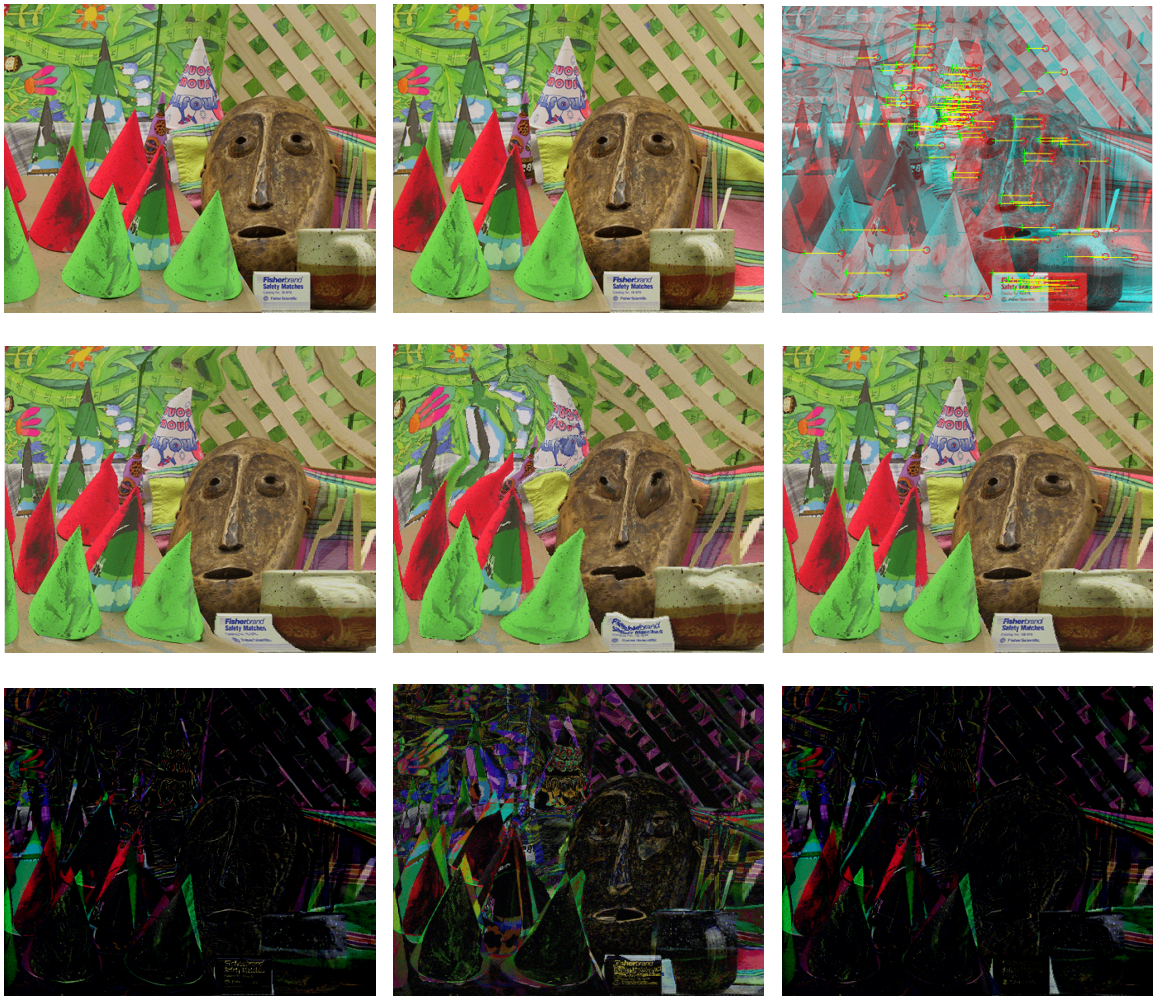

Fig. 15. Stereo landmark registration using different algorithms. Top left: The source image. Top middle: The target image. Top Right: The prescribed feature correspondences. Middle left: The registration result by the dense grid-based approach (4 pixels per grid). Middle: The registration result via DMesh [6]. Middle right: The registration result by our proposed coarse triangulation-based method. Bottom left: The intensity difference after the registration by the dense grid-based approach. Bottom middle: The intensity difference after the registration via DMesh [6]. Bottom right: The intensity difference after the registration by our proposed coarse triangulation-based method.

matching. SIAM Journal on Imaging Sciences, Volume 3, Issue 1, pp. 52–78, 2010.

[23] L. M. Lui, K. C. Lam, S. T. Yau, and X. Gu, *Teichmüller mapping (T-map) and its applications to landmark matching registration*. SIAM Journal on Imaging Sciences, Volume 7, Issue 1, pp. 391–426, 2014.

[24] L. M. Lui, K. C. Lam, T. W. Wong, and X. Gu, *Texture map and video compression using Beltrami representation*. SIAM Journal on Imaging Sciences, Volume 6, Issue 4, pp. 1880–1902, 2013.

[25] T. W. Meng, G. P.-T. Choi, and L. M. Lui, *TEMPO: Feature-endowed Teichmüller extremal mappings of point clouds*. Preprint, arXiv:1511.06624, 2015.

[26] A. Polesel, G. Ramponi, and V. J. Mathews, *Image enhancement via adaptive unsharp masking*. IEEE Transactions on Image Processing, Volume 9, Number 3, pp. 505–510, 2000.

[27] M. Rubinstein, D. Gutierrez, O. Sorkine, and A. Shamir, *A comparative study of image retargeting*. ACM Transactions on Graphics (Proceedings SIGGRAPH Asia 2010), Volume 29, Number 5, New York, NY, USA, 2010, pp. 160:1–160:10.

[28] J. R. Shewchuk, *Triangle: Engineering a 2D quality mesh generator and Delaunay triangulator*. Applied Computational Geometry: Towards Geometric Engineering, Volume 1148. Springer-Verlag, pp. 203–222, May 1996.

[29] R. Shi, W. Zeng, Z. Su, H. Damasio, Z. Lu, Y. Wang, S. T. Yau, and X. Gu, *Hyperbolic harmonic mapping for constrained brain surface registration*. IEEE Conference on Computer Vision and Pattern Recognition (CVPR), pp. 2531–2538, 2013.

[30] Y. Wang, L. M. Lui, X. Gu, K. M. Hayashi, T. F. Chan, A. W. Toga, P. M. Thompson, and S. T. Yau, *Brain surface conformal parameterization using Riemann surface structure*. IEEE Transactions on Medical Imaging, Volume 26, Number 6, pp. 853–865, June 2007.

[31] Y. Wang, L. M. Lui, T. F. Chan, and P. M. Thompson, *Optimization of brain conformal mapping with landmarks*. Proceedings of Medical Image Computing and Computer-Assisted Intervention (MICCAI), Part II, pp. 675–683, Oct. 2005.

[32] W. Zeng and X. D. Gu, *Registration for 3D surfaces with large deformations using quasi-conformal curvature flow*. IEEE Conference on Computer Vision and Pattern Recognition (CVPR), pages 2457–2464, 2011.

[33] W. Zeng, L. M. Lui, and X. Gu, *Surface registration by optimization in constrained diffeomorphism space*. IEEE Conference on Computer Vision and Pattern Recognition (CVPR), pages 4169–4176, 2014.

[34] B. Zitova and J. Flusser, *Image registration methods: A survey*. Image and Vision Computing, Volume 21, Issue 11, pp. 977–1000, 2003.